Acta Materialia 212 (2021) 116935

Contents lists available at ScienceDirect

Acta Materialia

journal homepage: www.elsevier.com/locate/actamat

Reversible Mn/Cr dual redox in cation-disordered Li-excess cathode materials for stable lithium ion batteries

Xuerong Zheng[a,b], Zhengrui Xu[a], Shaofeng Li[c], Yuxin Zhang[a], Jinfeng Zhang[b], Chunguang Kuai[a,b], Lei Tao[a], Muhammad Mominur Rahman[a], Yan Zhang[b,c], Sang-Jun Lee[c], Cheng-Jun Sun[d], Luxi Li[d], Wenbin Hu[b,*], Dennis Nordlund[c], Jue Liu[e], Yijin Liu[c], Feng Lin[a,*]

[a] Department of Chemistry, Virginia Tech, Blacksburg, VA 24061, United States
[b] Key Laboratory of Advanced Ceramics and Machining Technology of Ministry of Education, School of Materials Science and Engineering, Tianjin University, Tianjin 300072, China
[c] Stanford Synchrotron Radiation Lightsource, SLAC National Accelerator Laboratory, Menlo Park, California 94025, United States
[d] Advanced Photon Source, Argonne National Laboratory, Argonne, Illinois 60439, United States
[e] Neutron Scattering Division, Oak Ridge National Laboratory, Oak Ridge, Tennessee 37831, United States

ARTICLE INFO

Article history:
Received 2 February 2021
Revised 14 April 2021
Accepted 25 April 2021
Available online 1 May 2021

Keywords:
Disordered rocksalt
High rate capability
Long cycle life
Dual redox
Li ion battery

ABSTRACT

Cation-disordered Li-excess oxides/oxyfluorides have opened the door for designing alternative, high energy cathodes. However, achieving long cycle life and high rate capability represents a major challenge for disordered rocksalt cathodes (DRX). Herein, we develop $Li_2Mn_{3/4}Cr_{1/4}O_2F$ (LMCOF) DRX materials through a distinct redox mechanochemical method. The LMCOF contains trivalent Cr^{3+} and Mn^{3+}, which allows for simultaneously accessing stable Mn/Cr dual redox at a narrow voltage window acceptable for conventional carbonate electrolytes. Coupled with the mitigated and reversible oxygen chemical changes, the LMCOF delivers high capacity, rate capability, as well as long cycle life upon extensive 1,000 cycles at various current densities. The multiscale synchrotron and neutron scattering, spectroscopic, and imaging analyses demonstrate that the capacity originates from the Mn/Cr dual redox with minimal contribution from oxygen redox, and that the good cycle life is attributed to the stable global crystal structure and local oxygen chemical environment.

1. Introduction

The recent progress of disordered rocksalt chemistry has unlocked a vast chemical space for designing high capacity cathode materials, such as $Li_2Ni_{1/3}Ru_{2/3}O_3$ [1], $Li_{1.15}Ni_{0.45}Ti_{0.3}Mo_{0.1}O_{1.85}F_{0.15}$ [2], $Li_{4/3}Mo_{2/3}O_2$ [3], $Li_{1.25}Nb_{0.25}Mn_{0.5}O_2$ [4], $Li_{1.3}Nb_{0.3}V_{0.4}O_2$ [5], and $Li_{1.171}Mn_{0.343}V_{0.486}O_2$ [6] Li-excess disordered rocksalt oxides, and their fluorinated variants [6–11]. These materials can easily deliver material-level specific capacity and energy above 230 mAh g^{-1} and 700 Wh Kg^{-1}, respectively, which are at the upper bound of conventional stoichiometric layered oxide cathodes. The percolation theory, proposed to explain the electrochemical properties of these disordered rocksalt (DRX) cathode materials, suggests that the Li-excess environments in DRX enable efficient Li ion transport in three-dimensional (3D) percolating pathways [12–14]. 10% Li excess is a minimal prerequisite to form percolation networks to ensure efficient Li^+ migration in 3D channels [12,15]. Many DRX materials usually have high-valent transition metals (TMs) as charge compensators, such as Ti^{4+}, Zr^{4+}, Nb^{5+}, V^{5+}, and Mo^{6+}, which are redox inactive species and are difficult to be reduced or oxidized during electrochemical cycling [16–23]. Thus, the high-valent charge compensators inevitably reduce the redox active TM content in DRX compounds [19,24]. Therefore, one key aspect for designing DRX materials is to maximize the redox active TM content and thus its contribution to the overall capacity, without relying much on the anionic redox activity.

Another key aspect for developing DRX materials is to improve cycle life, which represents a critical step towards their large-scale applications. To date, almost all the reported DRX materials are hindered by the inferior cycling stability [25]. For example, Li_2VO_2F can deliver a high specific capacity of over 400 mAh g^{-1} and a specific energy of 1080 Wh kg^{-1} at C/60 and 1.3–4.1 V vs Li/Li^+ [26]. $Li_4Mn_2O_5$ can provide 355 mAh g^{-1} specific capacity and 953 Wh kg^{-1} specific energy at 25 mA g^{-1} and 1.2–4.8 V vs Li/Li^+ [27]. However, the capacity retention for Li_2VO_2F and $Li_4Mn_2O_5$ are only 70.4% after 8 cycles and 60% after 13 cycles, respectively [26,27]. Most recently, $Li_2Mn_{0.67}Nb_{0.33}O_2F$ and $Li_2Mn_{0.5}Ti_{0.5}O_2F$ were re-

* Corresponding authors.
E-mail addresses: wbhu@tju.edu.cn (W. Hu), fenglin@vt.edu (F. Lin).

https://doi.org/10.1016/j.actamat.2021.116935
1359-6454/

ported to provide specific capacity over 300 mAh g^{-1} at 20 mA g^{-1} and 1.5–5.0 V vs Li/Li^+. However, their capacity retention is about 60% after 25 cycles [13]. $Li_{1.2}Mn_{0.6}Nb_{0.2}O_{1.9}F_{0.1}$ showed a 92.4% capacity retention after 20 cycles at 10 mA g^{-1} and 1.5–4.8 V vs Li/Li^+. Therefore, these pioneering studies have laid the foundation for expanding the chemical space of DRX materials, but the cycle life upon extensive cycling needs further investigation [24]. Recent experimental and theoretical studies indicate that the inferior stability of DRX materials results from the deterioration of the 3D percolating network, possibly caused by irreversible oxygen redox and release, TM dissolution, and phase separation [28–31]. In Li-rich DRX oxides, O 2p orbitals in the Li-O-Li configuration cannot hybridize with TM d orbitals due to the large energy separation, thus the orphaned unhybridized O 2p states are susceptible to oxidation [32]. The oxygen loss can shrink the oxygen framework, accelerate the migration of under-coordinated TM ions, and create cation-densified surface to undermine Li ion kinetics and degrade the cycling performance [32–34]. Therefore, one may reduce the reliance on oxygen redox and focus on maximizing the TM redox activity to utilize the high capacity characteristics of DRX cathodes without compromising cycle life.

Herein, we design lithium manganese chromium oxyfluoride ($Li_2Mn_{3/4}Cr_{1/4}O_2F$, designated as LMCOF) containing trivalent Cr^{3+} and Mn^{3+} as dual redox species, which exhibits high specific capacity and energy, as well as good cycle life. We demonstrate, through a suite of synchrotron and neutron scattering, spectroscopic and imaging characterizations, that the good battery performance is attributed to the following factors: (i) the unique TM redox reactions during mechanosynthesis yield intermediate-valent Cr^{3+} and Mn^{3+} cations, which allows for accessing dual TM redox and reducing oxygen activity, (ii) the local TM and O chemical environments are stable and reversible, and (iii) the bulk crystal structure is stable and no phase separation is observed after 1000 cycles. Our mechanistic study enables us to propose strategies for enlarging the chemical design space of dual redox DRX materials and thus to establish new guidelines for developing cation-disordered cathodes.

2. Methods

2.1. Materials synthesis

To synthesize LMCOF, a stoichiometric amount MnO (Sigma Aldrich, 99%, 10.125 mmol), CrO_3 (Alfa Aesar, 99%, 3.375 mmol), LiF (Alfa Aesar, 98%, 13.5 mmol), and Li_2O (Aldrich, 97%, 8.4 mmol) were dispersed in Ar-filled ZrO_2 jars (50 mL). We added 10% excess Li_2O to compensate the possible loss during synthesis. The total amount of precursors was about 1.8 g. For ball milling, we use ten 10 mm-diameter and twenty five 5 mm-diameter ZrO_2 balls as the grinding media. The ZrO_2 jars were sealed using parafilm and then covered by duct tape to ensure good sealing and no air leakage during ball milling. All the procedures were carried out in an Ar-filled glove box. The ZrO_2 jars were transferred out of the glove box and ball-milled for 45 min with a rotation frequency of 38 Hz followed by a 10-min interval. The operation was repeated for 70 cycles to ensure the effective ball-milling time reaching 52 h. For synthesizing LMNOF and LMMOF, the same procedures were used and Nb_2O_5 and MoO_3 were used instead of CrO_3. The synthesized products were stored in the glove box for further utilization and characterization.

2.2. Phase structure, morphology and composition characterizations

The lab X-ray diffraction (XRD) was performed on a PANalytical *X*-ray diffractometer with Cu source at a scan rate of 2°/min. Synchrotron XRD was performed at the beam line 11–3 of Stanford Synchrotron Radiation Lightsource (SSRL) with a wavelength of 0.976 Å. The electrode samples were sealed between two Kapton tapes. LaB_6 sample was placed in the same location as the other samples and was used to calibrate the diffraction configuration. 2D MAR345 diffraction images were converted to 1D diffraction patterns based on the calibration parameters obtained from the LaB_6 diffraction pattern. The morphology of the powder and electrode was evaluated with scanning electron microscopy (SEM, FEI Quanta 600 FEG) and scanning transmission electron microscopy (STEM, JEM-ARM200F), equipped with an energy dispersive *X*-ray (EDX) detector. The inductively coupled plasma (ICP) instrument is a Spectro ARCOS SOP (side-on or radial view of the plasma interface) made by Spectro Analytical Instruments, Inc. X-ray total scattering experiments were carried out at the *X*-ray powder diffraction (XPD) beamline (28-ID-2) at the National Synchrotron Light Source II (NSLS-II, Brookhaven National Laboratory, USA), with a photon wavelength of 0.185794 Å. The diffraction patterns collected from the two-dimensional detector were radially integrated using Fit2D. The pair distribution functions, G(r), were extracted using PDFgetX3. Neutron total scattering data were collected at the Nanoscale-Ordered Materials Diffractometer (NOMAD) beamline at the Spallation Neutron Source (SNS) at Oak Ridge National Laboratory [35]. For the current experiment, about 0.3 g powder sample was loaded into a 3 mm quartz capillary. Four 30 min scans were collected for each powder sample and then summed together to improve statistics. The detectors were calibrated using scattering from a diamond powder standard prior to the measurements. Neutron powder diffraction data were normalized against a vanadium rod, the background (empty quartz capillary) was subtracted, and the total scattering structure factor S(Q) data were transformed to pair distribution function data G(r) using the specific IDL codes developed for the NOMAD instrument with the Q range of 0.2 to 25 $Å^{-1}$.

2.3. Operando *and* ex situ *hard X-ray absorption spectroscopy (XAS) characterizations*

Operando hard XAS measurements at the Mn and Cr K-edge were carried out at beamline 20-BM-B in the Advanced Photon Source (APS) at Argonne National Laboratory. For preparing the battery, we punched holes on the coin cell parts with a diameter of 2 mm and on the spacer with a diameter of 5 mm. The detailed description for assembling battery can be found in the later electrochemical measurement section. The holes on the two sides of the battery were sealed by Kapton tapes. Two aluminum wires were welded to each side of the battery. The battery was fixed on a homemade holder, connected to the electrochemical workstation, and cycled at current density of 100 mA g^{-1}. All measurements were performed in the transmission mode at room temperature using a Si(111) fixed-exit, double-crystal monochromator. The *ex situ* hard XAS was measured in the transmission mode at beamline 20-ID of the Advanced Photon Source at Argonne National Laboratory. The charged/discharged electrode films were sealed in Kapton tapes in an Ar-filled glove box. Energy calibration of each spectrum was made by aligning the first derivative maximum of reference Mn, Cr, Nb and Mo X-ray absorption near edge structure (XANES) spectra collected simultaneously from the metal foils in the reference channel. To determine the valence states of the transition metals at different states of charge, we selected the nearly linear portion of the rising edge for integration and defined the integrated average intensity as the K-edge [36,37]. Similar method was used to determine the K-edge position of the references of Mn and Cr and confirmed that the calculated K-edge values were in a linear relationship with the valence state. Here we use $LaCrO_3$ [38], CrO_2 [39] and $CaCr_{0.5}Fe_{0.5}O_3$ [40], where Cr cations are oc-

tahedrally coordinated, as Cr^{3+}, Cr^{4+}, and Cr^{5+}references, respectively, for quantifying the Cr valence state in the LMCOF. Similarly, MnO, Mn_2O_3 and MnO_2 are used as Mn^{2+}, Mn^{3+}, and Mn^{4+} references for Mn in the LMCOF. The calculated K-edges at different states of charge were then compared with the reference K-edges. The valence states can be determined based on the K-edge position shift relative to the references, and the corresponding capacity can also be obtained according to the calculated valence states using coulometry. We utilized the Fortran-based HAMA code to do the Morlet wavelet transforms (MWT) of k^2 weighted extended X-ray absorption fine structure (EXAFS) spectra [41,42]. For appropriate resolution in R- and k-space, we found a wavelet parameter combination of $k = 3$ and $\sigma = 2$ well suited to discriminate atomic contributions in the Fourier transforms of Mn and Cr K-edge EXAFS spectra.

2.4. RIXS and soft XAS characterizations

Resonant inelastic X-ray scattering (RIXS) measurements were carried out at beamline 10–1 at the SSRL using transition edge sensor (TES) spectrometer, which is the leading detector technology for nuclear materials analysis, sub-mm and mm-wave astrophysics, and X-ray experiments. The TES spectrometer consists of a 240-channel energy-dispersive detector array facing the sample-*X*-ray interaction point at 90° with regards to the incoming *X*-ray beam. The distance between the interaction point and the TES detector array was 5 cm. To achieve higher energy resolution of the TES than in a normal operation mode, only a subset of the detector array (64 pixels) was employed during the O K-edge RIXS measurements, and each O K-edge was scanned at least 10 times to get signal with good resolution. The energy measured by the TES was calibrated through separate measurements of a reference sample consisting of C, N, O, and various transition metal oxides with known emission energies. Sample exposure to the air was minimized using N_2-filled glove bags during the sample mounting, and the samples were measured under ultra-high vacuum (UHV) chamber. No sign of radiation damage was observed in the RIXS measurements based on no noticeable change in the measured spectral shape between consecutive scans.

Soft XAS measurements were performed on the 31-pole wiggler beamline 10-1 at SSRL using a ring current of 350 mA and a 1000 L mm^{-1} spherical grating monochromator with 20 μm entrance and exit slits, providing ~10^{11} pH s^{-1} at 0.2 eV resolution in a 1 mm^2 beam spot. The electrodes were harvested from a conventional coin cell and was dried before measurements in the ultra-high vacuum environment. The samples were mounted on an aluminum sample holder with double-sided carbon tape in an Ar-filled glove box and transferred to the UHV chamber and measured at room temperature using fluorescence yield (FY) mode. All spectra were normalized by the current from freshly evaporated gold on a fine grid positioned upstream of the main chamber.

2.5. X-ray fluorescence mapping (XFM) characterization

XFM were performed at the microprobe hard *X*-ray 2-ID-D beamline at the APS. The samples are raster-scanned by a submicrometer focused *X*-ray beam with 10 keV photon energy. The fluorescent *X*-rays are detected by a single element Si-drift Vortex detector. The schematic of the experimental setup can be found in [43]. The raw data is processed and quantified by MAPS. All images presented in this work covers a 100 μm × 100 μm area with 0.5 μm × 0.5 μm pixel size.

2.6. Electrochemical measurements

For preparing the cathode, 280 mg active material and 80 mg carbon black were ball-milled in Ar-filled ZrO_2 jars at 30 Hz for 3 h with ten 10 mm-diameter and twenty five 5 mm-diameter ZrO_2 balls as the grinding media. Then, polytetrafluoroethylene (PTFE, 10%) was added in a mortar as the binder and the weight ratio of active material, carbon black and PTFE is 7:2:1. The mixture was grinded for 30 min before being rolled into thin film. The thin film was overturned for several times to make it more evenly and more elastic. The cathode was then cut into disks of 6 mm in diameter, with an active mass loading of 3–4 mg/cm^2. All of the procedures were performed in an Ar-filled glove box. To assemble a cell for battery testing, 1 M $LiPF_6$ in 3:7 wt ratio of ethylene carbonate/ethyl methyl carbonate with 2 wt.% vinylene carbonate (EC/EMC = 3:7, VC 2%) solution, glass microfiber (Whatman® GF/D) and Li metal foil were used as the electrolyte, separator and anode, respectively. Coin cells (CR2032) were assembled in an Ar-filled glove box and tested on a Wuhan Land battery testing system at 22 °C. For the galvanostatic intermittent titration technique (GITT) measurements, the cell was charged/discharged at a current density of 50 mA g^{-1} for 60 min, followed by relaxation for 5 h to reach a quasi-equilibrium state. Such process is repeated until the charging/discharging cutoff voltage was reached. For preparing prelithiated anodes, firstly, oxygen-enriched lignin-derived carbon membranes (OLCM) were fabricated by electrospinning lignin-based resin solution, carbonization and oxidation. Then, the obtained OLCM was directly cut into disk (10 mm diameter) as the host to accommodate Li metal. The coin cells (CR2032) were assembled in an Ar-filled glove box using Li foils as counter/reference electrodes, glass microfiber (Whatman® GF/D) as separators, OLCM as working electrodes. The cells were cycled at 0–1.0 V vs Li/Li^+ and 0.2 mA cm^{-2} for 5 cycles for activation. Then 4.71 mAh cm^{-2} metallic Li was plated onto the electrode at a constant current of 1.0 mA cm^{-2} (**Fig. S1**). Actually, the loading mass of the metallic Li that can participate in the electrochemical reaction is much less than 4.71 mAh cm^{-2} due to the reaction between Li and electrolyte forming non-metallic Li compounds during battery cycling. The prelithiated anodes were retrieved by disassembling the coin cell in an Ar-filled glove box. The full cells were assembled using the LMCOF cathodes and the prelithiated anodes with the same procedure as assembling half cells. The specific capacity was calculated on the loading of the active material in the cathode.

3. Results and discussion

3.1. Synthesis and characterization of $Li_2Mn_{3/4}Cr_{1/4}O_2F$

We synthesized LMCOF by mixing a stoichiometric amount of Li_2O, MnO, CrO_3 and LiF, followed by a mechanochemical ball milling process (see Experimental Methods). Nb and Mo are popular TMs in reported DRX materials [3,5,13], and they are in the vicinity of Cr in the periodic table. Thus, we also synthesized $Li_2Mn_{2/3}Nb_{1/3}O_2F$ (LMNOF) and $Li_2Mn_{3/4}Mo_{1/4}O_2F$ (LMMOF) as references to illustrate the distinct electrochemical properties of LMCOF. Synchrotron XRD (Figs. 1a and **S2**) and neutron diffraction (**Fig. S3, Table S1**) show that all the oxyfluorides form the typical disordered rocksalt structure with a Fmm space group, in which O/F anions form a cubic close-packed framework and Li/TM cations occupy the octahedral sites therein (**Fig. S4**). Inductively coupled plasma mass spectrometry (ICP-MS) confirms that the Li/TM stoichiometry is close to the designed $Li_2Mn_{3/4}Cr_{1/4}O_2F$ (**Table S2**). X-ray and neutron pair distribution function (PDF) analyses, powerful techniques for providing insights into the nanoscale crystal structure, are used to investigate the atomic structure of the LMCOF in different length scales (Fig. 1**b, Table S1**), and compared

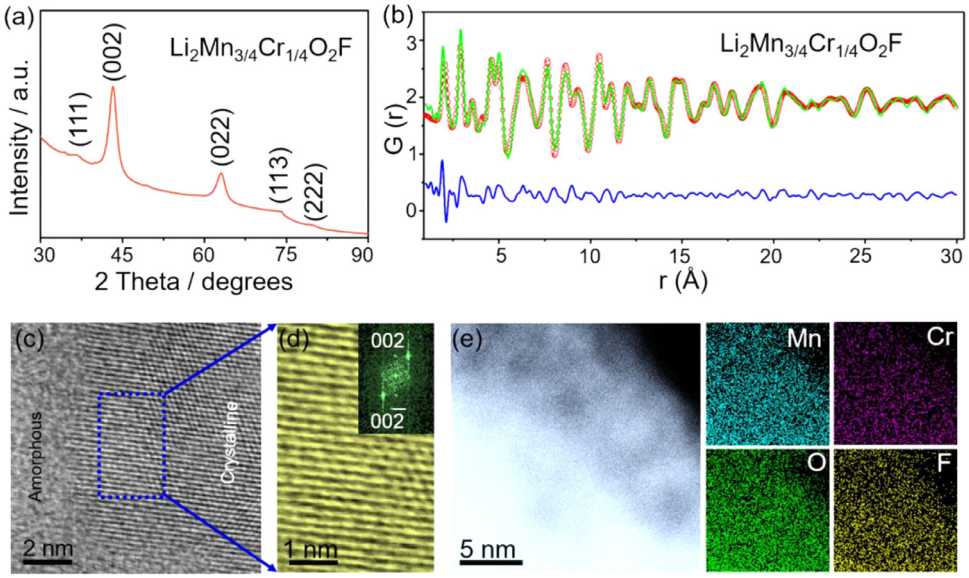

Fig. 1. (a) Synchrotron XRD pattern of the LMCOF, where the *X*-ray wavelength is calibrated to Cu K_α. (b) Least square refinement of a complete cation disordered model using *X*-ray PDF data: raw experimental data (black), refined model (red), and difference curve (blue). (c) HRTEM image containing amorphous and crystalline areas. (d) HRTEM image and FFT pattern (inset) of a crystalline nanodomain in the LMCOF particles. (e) Scanning transmission electron microscopy (STEM) -EDS elemental mapping of Mn, Cr, O, and F in the LMCOF, where all constituting elements are present in the same particle (For interpretation of the references to color in this figure legend, the reader is referred to the web version of this article.).

with the other two products (**Figs. S5 and S6**). Generally, almost all the X-ray PDF peaks for the three products can be well fitted in the long r range of 10–30 Å, suggesting the consistency with the average cation disordered rocksalt structure (**Fig. S5a**). However, in the short r range (0.5–10 Å) especially for the two peaks standing at 1.6 and 3.1 Å (**Fig. S5b**), the average cation disordered model cannot adequately describe the observed structure features. The fit for LMCOF is noticeably better than the fits for LMMOF and LMNOF. The refined residual (R_w) value of LMCOF (25.77%) is smaller than those of LMNOF (35.97%) and LMMOF (39.44%), indicating that LMCOF likely possess more disordered structure (**Fig. S5**). This has been further confirmed by the small box refinement results of LMCOF and LMMOF using the neutron PDF data (**Fig. S6**). The more disordered structure in the LMCOF can be ascribed to two factors: (i) the charge difference between Li^+ and trivalent cations (Cr^{3+} and Mn^{3+}) is smaller than that between Li^+ and high valent cations of Nb^{5+} in LMNOF and Mo^{6+} in LMMOF, indicating lower Coulombic force driving Cr^{3+}/Mn^{3+} to minimize the electrostatic energy (Note: the presence of Cr^{3+}/Mn^{3+} cations will be discussed in the next section); (ii) Mn^{3+} (high spin d^4) is a strong Jahn-Teller distortion cation, demonstrating LMCOF has stronger Jahn-Teller distortion of Mn^{3+}-octahedra [44–46]. The combination of these two driving forces may result in more disordered patterns in LMCOF. The highly disordered structure was reported to benefit the structural stability and immutability of Li^+ local environment upon (de)lithiation [25]. Thus, it is anticipated that LMCOF may exhibit more stable crystal structure upon electrochemical cycling.

SEM, TEM and high resolution TEM (HRTEM) images show that the LMCOF polycrystalline particles are in the range of 100–200 nm, consisting of 8–15 nm crystalline nanodomains (**Fig. S7**). Moreover, a considerable amorphous structure can be observed in the HRTEM image (**Figs. 1c and S7c-d**), indicating that the LMCOF are composed of crystalline and amorphous nanodomains. The exposed facet and crystallographic characteristics of LMCOF are revealed by the HRTEM image and the corresponding fast Fourier transform (FFT, inset in **Fig. 1d**). The energy dispersive spectroscopy (EDS) elemental mapping confirms that Mn, Cr, O, and F are co-present in the bulk phase, both in crystalline and amorphous areas (**Fig. 1e**). In summary, the microstructural characterization implies that the LMCOF contains a notable proportion of amorphous nanodomains and displays a low crystallinity and a high degree of disorder, which is different from many reported, high-crystalline DRX materials [12,14,17].

3.2. Structural and electronic evolution of $Li_2Mn_{3/4}Cr_{1/4}O_2F$ during redox mechanochemical synthesis

Understanding how the multicomponent precursors are transformed to the LMCOF during mechanochemical synthesis may offer insights into identifying the unique structural and electronic attributes of this new material. We performed hard XAS to analyze the electronic structures of Cr and Mn in the as-synthesized LMCOF. The hard XAS spectra show that the as-synthesized LMCOF is mostly populated with cations close to Cr^{3+} and Mn^{3+} (**Fig. 2a**), indicating that Cr^{6+} is reduced and Mn^{2+} is oxidized during ball milling. Next, we quantitatively calculate the valence states of Cr and Mn and find that the average valence states of TMs are $Cr^{3.1+}$ and $Mn^{2.9+}$ (**Fig. 2b-c**, the detailed calculation method is discussed in Experimental Methods). To systematically track the redox process between Cr and Mn during mechanosynthesis, we performed hard XAS and XRD at different stages of ball milling to characterize the chemical and phase transformations from precursors to LMCOF (**Figs. 2d** and **S8**). The Cr pre-edge intensity gradually decreases and the K-edge experiences red shift with increasing reaction time, indicating the gradual reduction of Cr^{6+} to lower valence states. In contrast, Mn K-edge exhibits gradual blue shift upon ball milling, demonstrating the oxidation of Mn^{2+} towards higher valence states. The transformation to disordered rocksalt LMCOF is completed after 48 h of ball milling (**Fig. S8**). Since both Cr and Mn are nearly in the trivalent state, we hypothesize that Cr and Mn are both redox active and that LMCOF has the potential to become a promising cathode material. The theoretical redox capacity based on Cr^{3+}/Cr^{6+} and Mn^{3+}/Mn^{4+} redox couples can reach 329 mAh g^{-1}. Therefore, we further investigated the battery performance of LMCOF.

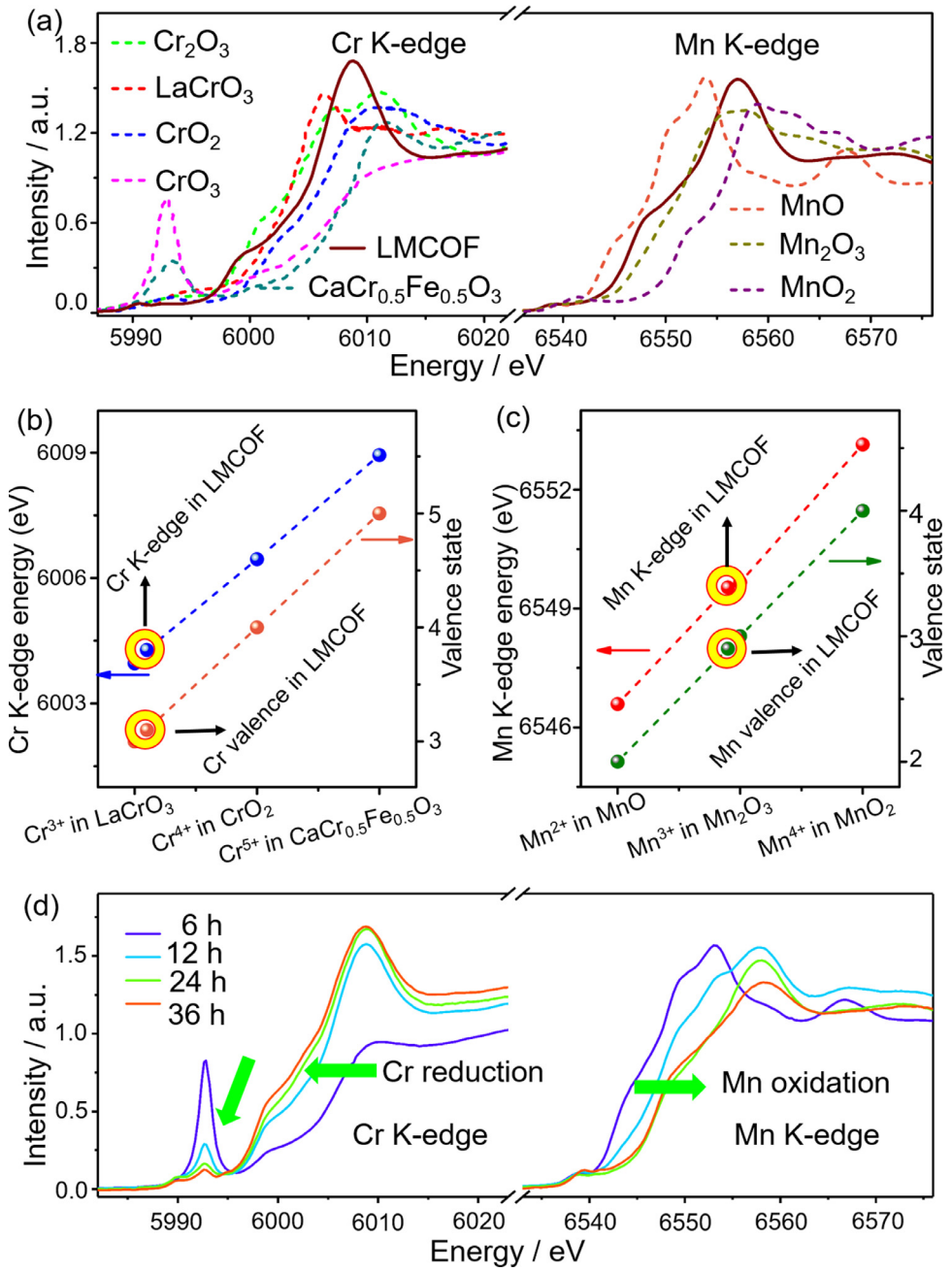

Fig. 2. (a) The Cr and Mn K-edge hard XAS in the pristine LMCOF, with reference spectra included for comparison (Cr^{3+}: $LaCrO_3$, Cr^{4+}: CrO_2, Cr^{5+}: $CaCr_{0.5}Fe_{0.5}O_3$, Cr^{6+}: CrO_3, Mn^{2+}: MnO, Mn^{3+}: Mn_2O_3, Mn^{4+}: MnO_2.). The Cr^{3+}, Cr^{4+} and Cr^{5+} reference spectra were extracted from Ref. [38, 39 and 40], respectively [38–40]. The calculation of (b) Cr and (c) Mn valence states using the edge energy determined by averaging the linear rising edge of hard XAS spectra, as described in the Experimental Method. (d) The evolution of Cr and Mn K-edge hard XAS during the redox mechanosynthesis of the LMCOF, where Cr and Mn undergo gradual reduction and oxidation, respectively. The measurements were all performed at room temperature.

3.3. Electrochemical performance of $Li_2Mn_{3/4}Cr_{1/4}O_2F$

Developing DRX materials with high capacity and energy, long cycle life, and high rate capability represents a critical path towards promoting their applications. The LMCOF delivers a high specific discharge capacity of 258 mAh g^{-1}, specific energy of 832 Wh Kg^{-1}, and a capacity retention of 57.6% after 500 cycles at 2.0–4.4 V and 50 mA g^{-1} (**Fig. 3a,b**). Increasing the current density to 200, 500 and 1000 mA g^{-1}, the batteries deliver small decrease of specific capacity and energy, and all the retention performance are well over 60% after 1000 cycles (**Figs. 3a-b and S9a-b**), as summarized in **Table S3**. It is worth noting that the capacity fading mainly occurs in the first 50 cycles, and the retention performance is much better beyond 50 cycles, with only 0.03% capacity fading averagely per cycle. The Coulombic and energy efficiency delivered by the LMCOF are also quite stable at different current densities (**Fig. S9c,d**). We have highlighted the advantages of our materials by directly comparing LMCOF with other reported cathodes (**Table S4**). The Cr^{3+} in LMCOF is expected to play a critical role for enhancing the specific capacity, specific energy, and cycling durability. Therefore, the Cr-containing oxides (DRXs and other structures) were presented in Table S4 for comparison. The results demonstrate that the cycle life of LMCOF is promising as a DRX material. **Fig. 3c** shows the voltage drop and jump

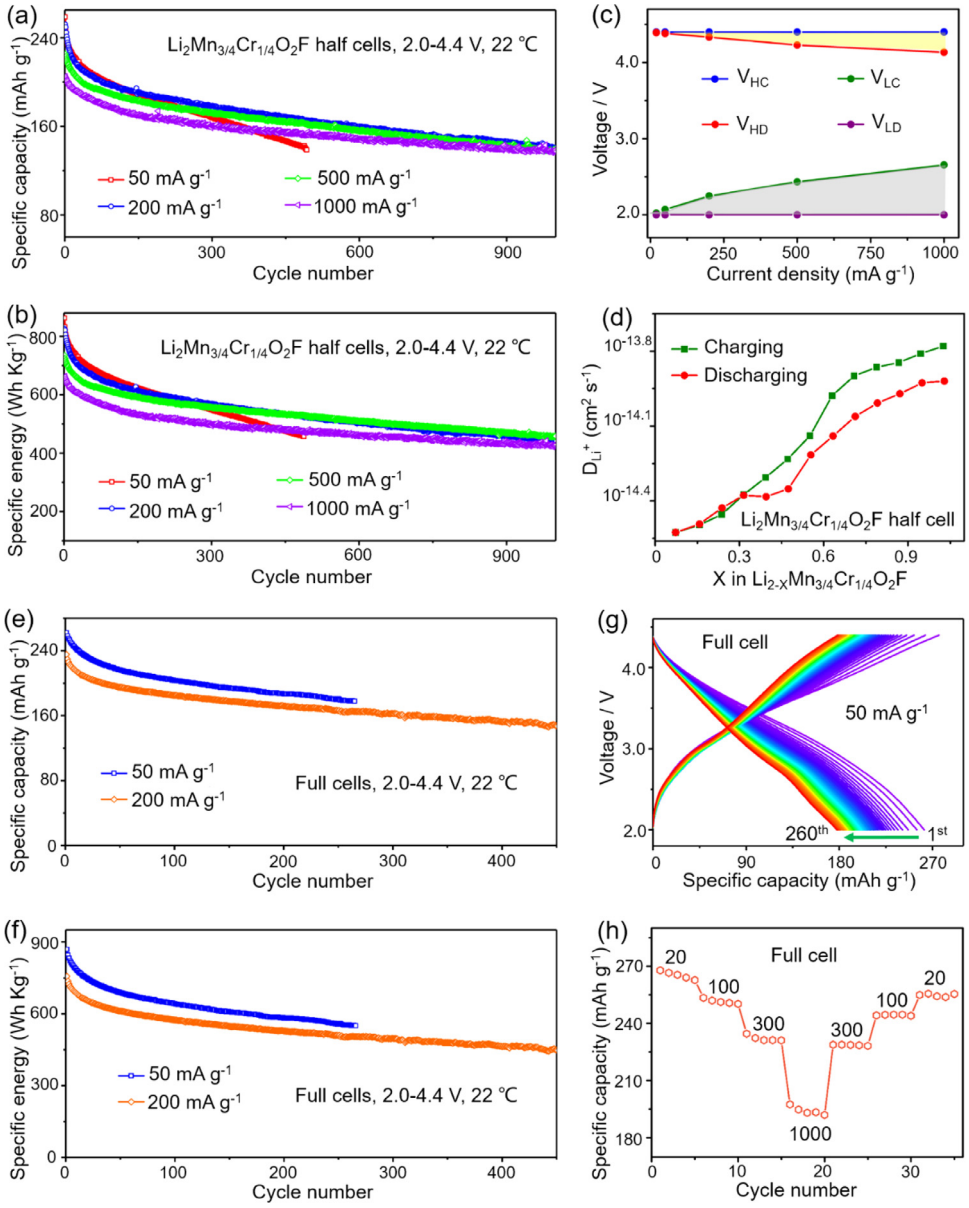

Fig. 3. (a) Specific discharge capacity of the LMCOF half cells measured at 50, 200, 500 and 1000 mA g^{-1} in 2.0–4.4 V vs. Li/Li^+. (b) The corresponding specific energy of the same cells shown in (a). (c) The voltage drop and jump at the second cycle of the LMCOF half cells as a function of current density. V_{HC} is the upper cutoff voltage of the cell (i.e., 4.4 V vs. Li/Li^+). V_{HD} is the starting discharge voltage. The difference between the two, labeled as the yellow shade, represents the voltage drop at the upper cutoff. Similarly, V_{LD} is the lower cutoff voltage of the cell (i.e., 2.0 V vs. Li/Li^+). V_{LC} is the starting charging voltage. The difference between the two, labeled as the gray shade, represents the voltage jump at the lower cutoff. The example is shown in **Fig. S10**. (d) Li ion diffusion coefficient in the LMCOF at different states of charge and discharge in the first cycle at 2.0–4.4 V vs. Li/Li^+determined by GITT. (e) The specific discharge capacity and (f) specific discharge energy of OLCM@Li||LMCOF full cells cycled at 50 and 200 mA g^{-1} in 2.0–4.4 V vs. Li/Li^+ at 22 °C. (g) The charge-discharge profiles of the OLCM@Li||LMCOF full cell cycled at 50 mA g^{-1}. (h) Rate capability performance of the OLCM@Li||LMCOF full cell. The OLCM@Li is a pre-lithiated carbon anode, with 4.71 mAh cm^{-2} Li loading in the carbon matrix. The detail information is discussed in Experimental Methods. (For interpretation of the references to color in this figure legend, the reader is referred to the web version of this article.)

of the LMCOF half cells at the beginning/end of charge/discharge at different current densities, as illustrated in **Fig. S10**. Particularly, the voltage drop of V_{HC}-V_{HD} remains relatively small when increasing the current density from 20 to 1000 mA g^{-1}. The small voltage drop at the upper voltage cutoff (**Figs.3c** and **S10**) reveals the fairly good stability and rate capability of LMCOF at high current densities [1]. The GITT result (**Fig. 3d**) shows that the Li^+ diffusion coefficient in LMCOF reaches 10^{-14}–10^{-13} cm^2/s, which is higher than other DRX materials[18] and some layered oxides [47,48], such as $Li_{1.2}Ni_{0.15}Co_{0.1}Mn_{0.55}O_2$ (10^{-17}–10^{-14} cm^2/s)[47] and $Li[Li_{0.23}Co_{0.3}Mn_{0.47}]O_2$ (10^{-18}–10^{-14} cm^2/s) [48].

Next we assembled full cells using prelithiated OLCM (OLCM@Li) as anodes (see Experimental Methods) [49]. When cycled at 50 and 200 mA g^{-1}, the OLCM@Li||LMCOF full cells deliver specific discharge capacity of 257 and 233 mAh g^{-1} (**Fig. 3e** and **g**), specific energy of 859 and 776 Wh kg^{-1} (**Fig. 3f**), capacity retention of 67.5% after 270 cycles and 57.9% after 450 cycles (**Figs. 3e** and **S11a**), respectively. The OLCM@Li||LMCOF full cells also exhibit reasonably good rate capability (**Fig. 3h**) and Coulombic efficiency (**Fig. S11b**). The performance of OLCM@Li||LMCOF full cells is comparable with the half cells containing bulk Li metal as the anodes (**Fig. 3a-b**).

Furthermore, we compare the battery performance of LMCOF with that of other DRX materials, such as LMNOF and LMMOF, under the identical electrochemical conditions. LMCOF exhibits considerably better specific capacity, energy and cycle life than LM-

MOF and LMNOF (**Fig. S12**). We also compared the battery performance of LMCOF with other DRXs that contains Mn^{3+} or Cr^{3+} species (**Fig. S13**). It is clear that LMCOF displays comparable or even better specific capacity and cycle life than most of these DRXs. The highly disordering structure in DRX materials is found to positively impact the battery performance [14,25]. We also confirm that the LMCOF possess a higher degree of disordered structure than LMNOF and LMMOF (**Fig. S5**). Another difference between LMCOF and other DRX materials is that the valence states of TM species in LMCOF are nearly trivalent ($Cr^{3.1+}$ and $Mn^{2.9+}$), and there may be Mn/Cr dual redox during cycling. However, the Nb^{5+} and Mo^{6+} charge compensators in LMNOF and LMMOF are electrochemically inactive during cycling, as confirmed by hard XAS shown **Fig. S14** and discussed later. Therefore, the higher degree of disordering structure and Mn/Cr dual redox (more discussion later) may have enabled the superior performance of LMCOF.

Based on the above results, we propose that the high retention performance of LMCOF should be attributed to the fact that the Mn/Cr dual redox species can contribute more redox capacity at low voltages, thus eliminating the need of oxygen redox that typically occurs at high voltages [17,28,50]. This should also provide more stable local chemical coordination environments. In addition, the structural stability is likely another important contribution. In the following section, we discuss our *operando* and *ex situ* synchrotron analyses to investigate these hypotheses.

3.4. Chemical and structural evolution of $Li_2Mn_{3/4}Cr_{1/4}O_2F$ during cycling

We performed *operando* hard XAS to investigate the charge compensation mechanism of LMCOF upon battery cycling. Corresponding to the sampling points shown in **Fig. 4a**, both Mn and Cr K-edge XAS spectra exhibit blue shift during charging, and then return to the initial position after discharging (**Fig. 4b,c**), indicating Mn and Cr are dual redox active species and their redox reactions take place synchronously throughout the cycle. Furthermore, we calculated the Mn and Cr valence states at each state of charge (**Fig. 4d,e**). Based on the coulometry, we then calculated the capacity contributed by Mn and Cr during cycling (**Fig. 4f**). The calculated discharge capacity contributed by the Mn/Cr dual redox is ~198 mAh g^{-1}, indicating about 21.7% capacity (~ 55 mAh g^{-1}) is contributed by the oxygen redox. This result is also confirmed by the *ex situ* hard XAS of the LMCOF, where the discharge capacity from oxygen redox is ~ 22.8% (**Fig. S15**). For comparison, we also calculated the TM and oxygen redox capacity of LMNOF and LMMOF using the same method based on their respective hard XAS spectra (**Fig. S16**). We find that the oxygen redox contributed 42.4% (84 mAh g^{-1}) and 59.4% (101 mAh g^{-1}) to the capacity of LMNOF and LMMOF, respectively. The percentage of oxygen redox capacity in LMNOF and LMMOF is much larger than that in LMCOF. This phenomenon is consistent with the cyclic voltammetry (CV) results (**Fig. S17**). CV is a commonly used method to investigate the degree of oxygen redox involvement [17,28]. The rising feature around 4.4–4.7 V is often attributed to the environmental change or the oxidation of O^{2-}, and the continuous decrease in the intensity suggests the irreversibility of the oxygen redox [17,28]. Comparing the CV profiles of LMCOF with those of LMNOF and LMMOF (**Fig. S17**), the oxygen redox feature (~ 4.4 V) for LMCOF is well repeated and weaker than those of LMNOF and LMMOF. This suggests that only a trace amount of oxygen redox contributes to the capacity in the LMCOF and its contribution is reversible. Therefore, less oxygen redox is triggered in the LMCOF during cycling at 2.0–4.4 V, which might have benefited the cycle life of this material in half and full cells.

To further substantiate this interpretation, we performed Morlet wavelet transform (MWT) analyses for Mn and Cr based on the k^2-weighted EXAFS at different states of charge and discharge (**Fig. 4g–l**). MWT is a powerful method to qualitatively identify the local structure and bonding environment of metal complexes by directly visualizing all the EXAFS contributions at once. It is also an efficient way for the identification of overlapping contributions in EXAFS signals that come from neighboring atoms with multiple-scattering [42,51,52]. The two maxima in the MWT image of Mn in pristine LMCOF (**Fig. 4g**) correspond to the first two coordination shells of O and TM around Mn atom, as the arrows marked in **Fig. 4g**. Upon charging to 4.4 V, the TM-O signal keep stable, while the TM-TM signal becomes weaker, and some additional weak TM-TM maxima appeared, marked by the arrows in **Fig. 4h**. This should be attributed to the multiple-scattering effects of neighboring oxidized TM atoms after charging (**Fig. 4h**) [42,51,52]. After discharging, the maxima signals return to their initial states (**Fig. 4i**). The MWT images of Cr also demonstrate the well reversibility of Cr coordination environment after discharging (**Fig. 4j-l**). The MWT results confirm the dual redox of Mn and Cr, and also demonstrate the good reversibility of local coordination environments for O and TMs during cycling.

Recently, Chen and coworkers reported that oxygen redox, especially oxygen release, as well as the structural and chemical degradation should be responsible for the battery performance deterioration [28]. Here we performed synchrotron XRD to investigate the structural evolution of LMCOF at different states of charge and discharge as well as after long-term cycles. As shown in **Fig. S18a,b**, the diffraction peaks exhibit a positive shift of only $2\theta = 0.3°$ when charged to 4.4 V and then shift back to the initial state after discharging to 2.0 V, suggesting a minor change of lattice parameter and good reversibility of the crystal structure. For the LMNOF, however, the positive shift range reaches $2\theta = 0.6°$ upon charging (**Fig. S18c,d**), which is much larger than that of LMCOF. In addition, the crystal structure of LMCOF remains fairly reversible and no new phase appear even after the capacity had faded to 60% retention (about 1000 cycles, **Fig. S18e,f**). Therefore, the LMCOF is distinct from many reported DRX materials where secondary phases can form in a short period of cycling (tens of cycles) [17,28]. It is also noted that such a good cycle life (60% capacity retention after 1000 cycles) may be adequate for certain practical applications.

Considering the close relationship between oxygen chemical environment and battery stability for long-term cycling [9,13,17,25,27–31], we investigate how the oxygen chemical environment evolves during cycling using synchrotron *X*-ray core-level spectroscopy. RIXS, with a probing depth of over 150 nm (i.e., bulk sensitive for the nanosized LMCOF particles) [53], has been shown effective in resolving the oxygen chemical environment, including oxygen redox activity. RIXS works by probing specific *X*-ray emission energy at a particular excitation energy [48,53]. Using this technique, here we identify the reversible oxygen chemical environment in the LMCOF. For the pristine LMCOF (**Fig. 5a**), the O K-edge RIXS map is composed of two features centered at about 530.5 and 534 eV, respectively [54]. Compared with the pristine sample, the RIXS maps of the half and fully charged LMCOF exhibit an increasing intensity at 530.5 eV and a decreasing intensity at 534 eV (**Fig. 5a-c**), indicating the increasing TM-O covalency upon charging. This is a typical phenomenon observed in cathode materials with TMs as the main redox active sites [53–57]. However, we do not observe the typical feature of peroxo-like species in the RIXS map of fully charged LMCOF [48,53], demonstrating the oxygen O^{2-} is only weakly oxidized and cannot be oxidized to a higher valence state, such as O_2^{2-} or O_2 species. In other words, it is plausible that the oxygen redox is weak and its RIXS signal contribution is overrun by the TM-O covalency signal. After one complete cycle (**Fig. 5e**), the critical features of the RIXS map restore, verifying the reversibility of the oxygen chemical environment. The evolution of the oxygen chemical environment in the RIXS maps are

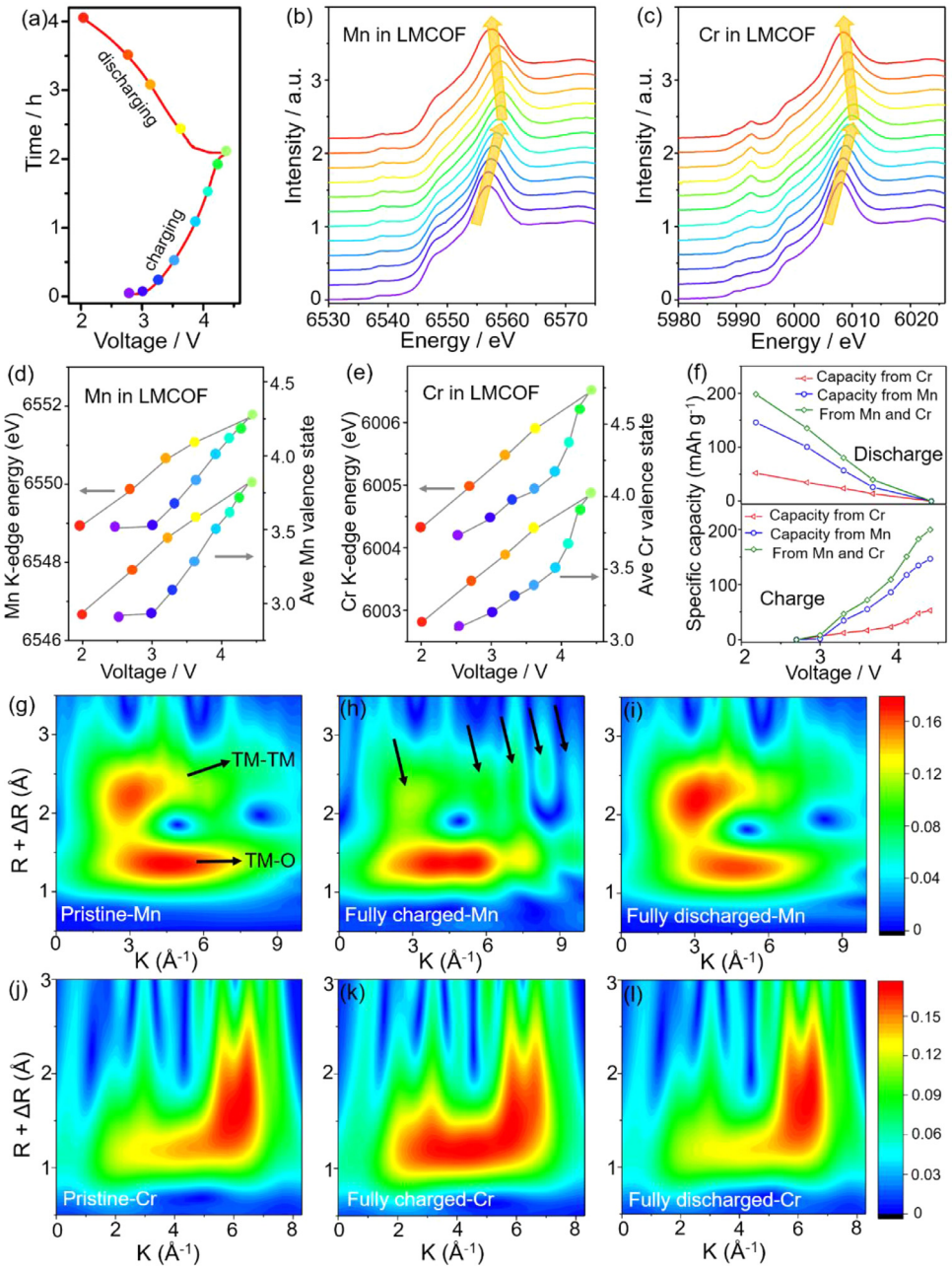

Fig. 4. (a) The charge-discharge profile of the *operando* LMCOF half cell at 100 mA g^{-1}, with the sampling points labelled in different colours corresponding to the color scheme shown in (b) and (c). The *operando* hard XAS spectra of (b) Mn and (c) Cr in the LMCOF during the initial cycle. The K-edge positions and valence states of (d) Mn and (e) Cr that are calculated by averaging the linear rising edge of the hard XAS spectra. (f) The calculated contribution of the Mn and Cr redox to the capacity. The Morlet wavelet transforms of k^2-weighted EXAFS spectra of the LMCOF in the first cycle of Mn K-edge at (g) pristine, (h) charged to 4.4 V, (i) discharged to 2.0 V, and Cr K-edge at (j) pristine, (k) charged to 4.4 V, (l) discharged to 2.0 V. The arrows in (g) indicate the first two coordination shells of O and TM around Mn atom. The arrows in (h) indicate the newly appeared maxima after charging. The measurements were all performed at room temperature.

consistent with the super-partial fluorescence yield (sPFY) signal (**Fig. 5f**). To track the oxygen stability in the LMCOF upon cycling, we performed soft XAS in the FY mode (probing ~50 nm) on the LMCOF after 50 cycles (LMCOF-50, **Fig. 5g**). Interestingly, no noticeable changes can be observed for the O K-edge spectra upon charging and discharging, indicating that no oxygen redox participate in the reaction and that only Mn and Cr redox contribute to the capacity after 50 cycles. It is also likely that the surface undergoes gradual degradation and becomes passivated after 50 cycles, a phenomenon that is widely reported for various oxide cathode materials [25,53–60]. Collectively, the RXIS and soft XAS results may explain the oxygen reversibility in the LMCOF and the faster capacity fading in the first 50 cycles than the subsequent cycles.

Finally, we investigated the capacity fading mechanism at the first 100 cycles for the LMCOF-based Li-ion batteries. We conjecture that this phenomenon might be related to the TM dissolution. The hard XAS results (**Fig. S20a,b**) show that the Cr K-edge position keep stable even after 100 cycles. However, the Mn K-edge spectra display positive shift upon extending cycling, suggesting the valence state of Mn increased in LMCOF. Then, we performed XFM to analyze the Cr and Mn deposition on the lithium anode (**Fig. S20c–e**), which is highly sensitive to quantitatively evaluate TMs at the sub-ppm level. The range of the Mn concentration on

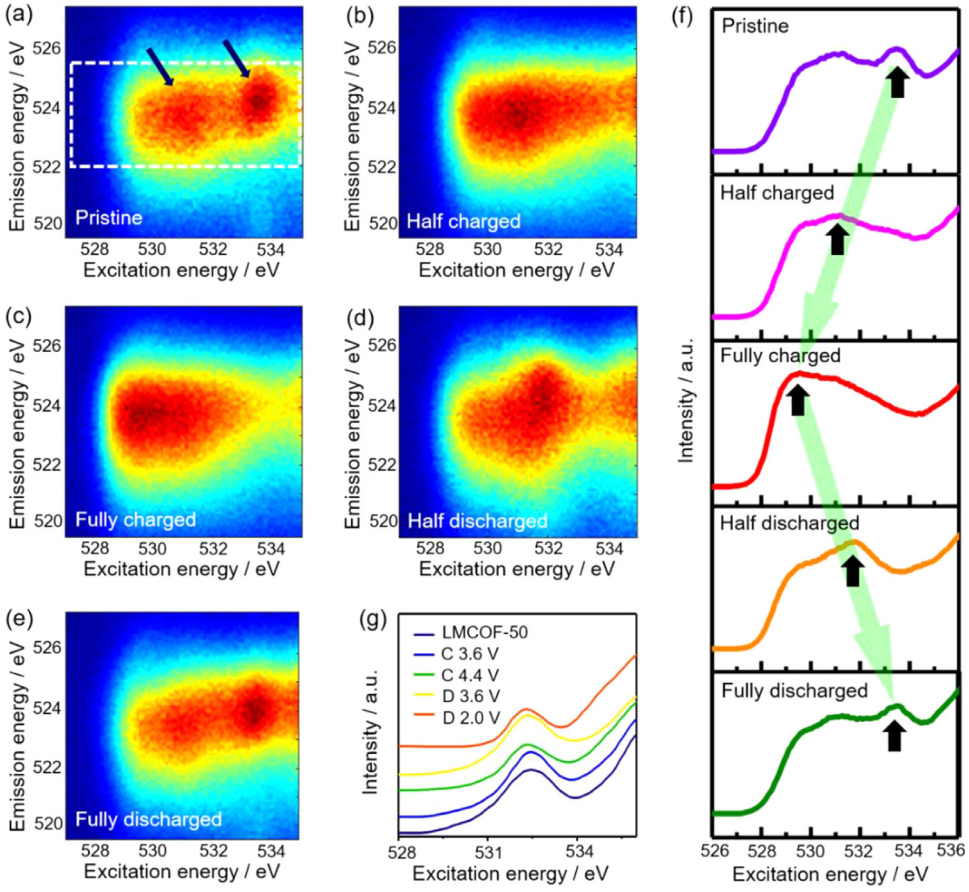

Fig. 5. Oxygen RIXS mapping on the LMCOF electrodes at different states of charge/discharge: (a) pristine, (b) half charged (137 mAh/g, 3.6 V vs. Li/Li^+), (c) fully charged (284 mAh/g, 4.4 V vs. Li/Li^+), (d) half discharged (123 mAh/g, 3.2 V vs. Li/Li^+), and (e) fully discharged (257 mAh/g, 2.0 V vs. Li/Li^+). The current density is 20 mA g^{-1} and the voltage profile is shown in **Fig. S19**. (f) The super-partial fluorescence yield (sPFY) signal extracted by vertically integrating the signal across a super-partial range marked by the dashed frames in (a) for the LMCOF electrode at different states of charge/discharge. The measurements are all performed at room temperature. (g) O K-edge soft XAS spectra of LMCOF after 50 cycles (LMCOF-50) and then charge/discharge to different voltages.

the anode is 0.5–7.0 $\mu g/cm^2$, and the mean value is 3.7 $\mu g/cm^2$ (67.3 nmol/cm^2) after 100 cycles. However, only trace amount of Cr can be detected after 100 cycles. Therefore, to keep the electroneutrality, the Mn in the lattice of LMCOF would be oxidized when part of Mn gets dissolved in the electrolyte after cycling. Moreover, we excluded the potential effect of the anode side by reassembling the LMCOF (after 20 cycles) with new anodes. The results (**Fig. S21a**) show that the reassembled battery could essentially continue the capacity and stability trend compared with the original ones, suggesting the anode has no major influence on the capacity degradation of LMCOF in the initial cycles. In addition, the TEM, HRTEM, and XRD were performed on the LMCOF that has finished 50 cycles (**Fig. S21b**). The diffraction peaks become weakly broader, demonstrating the slightly decreased crystallinity of LMCOF after initial cycling. However, as confirmed in **Fig. S18**, the main cubic structure can keep stable during long-term cycling.

3.5. Discussion

TM cations and Li^+ randomly occupy the octahedral sites in DRXs, which have long-range disordered but often short-range ordered (SRO) structures, and the Li^+ transport through the percolation structure of so-called "0-TM" channels during battery cycling. Traditional strategies, such as doping and coating, have no obvious effect on enhancing the stability of DRXs [61,62]. The oxygen redox, especially oxygen loss, has very close relationship with the stability of DRXs, because it can cause surface densification and trigger TM dissolution. We propose that combining two or more TM redox couples in one DRX and tunning the F content should be an opportunity for improving specific capacity, minimizing anion redox, and enhancing battery stability. This is because different TM redox couples can be triggered at their corresponding voltages. The combination of two or more TM redox centers can optimize the average redox voltage, thus probably reducing or even avoiding the involvement of oxygen redox especially at high charging voltages. Moreover, moderate F incorporation could reduce the oxygen redox activity, lower the valence states of TMs, and modulate the electronic structure of TMs, thus enhancing the theoretical capacity and stability of DRXs. In addition, as shown in this work, inactive d^0 TMs is not a prerequisite for forming disordered rocksalt structure and can be replaced by active TMs, which could increase the content of redox active TMs and improve theoretical capacity. Therefore, designing DRX materials with dual or more TM redox species provides an important avenue to further enhance battery capacity and retention performance.

We expect to see further optimization by strategically coupling different redox active species in one material, such as Mn-V, Fe-Cr and Fe-V systems, which may open a large chemical space for designing new cathode materials. Therefore, it seems necessary to first identify the suitable combination of dual redox TM cations. Our study indicates that two prerequisites may be needed for synthesizing dual redox DRX materials: (i) the charge compensators (e.g., Cr^{6+} in CrO_3 here) have labile d states and become stable in the synthesized species (e.g., Cr^{3+} with d^3 state); (ii) the TM ions

(such as Mn^{2+}) have a relatively small redox potential, which is beneficial for the redox reaction between TM and charge compensators. As in the LMCOF, the Cr^{3+} with a $3d^3$ state is more stable than Cr^{6+} with a $3d^0$ state [63,64], facilitating the redox reaction between Cr^{6+} and Mn^{2+} to form Cr^{3+}/Mn^{3+}dual redox species. In contrast, the Mo^{6+} ($3d^0$) and Nb^{5+} ($3d^0$) are inactive species with stable states in the MoO_3 and Nb_2O_5 precursors, which cannot be reduced by Mn^{2+} during mechanosynthesis and thus remain d^0 states in LMMOF and LMNOF, respectively [13–15,19–21]. Moreover, Mn^{2+}/Mn^{3+} has a smaller redox potential than some other TM ions, such as Ni^{2+}/Ni^{3+} [65–67]. We preliminarily investigate this speculation in one aspect by designing a synthesis using NiO and CrO_3 as precursors. As expected, Ni^{2+} cannot be oxidized during mechanosynthesis and no pure DRX phase can be obtained following the same synthesis protocol established in the work (**Fig. S22**), indicating no redox reaction takes place between Ni^{2+} and Cr^{6+}. Similarly, as shown in **Fig. S23**, no pure LMCOF DRX phase is formed when we use Mn_2O_3 and Cr_2O_3 as the precursors. We anticipate that more studies would be needed to further understand the importance of redox reactions during mechanosynthesis.

4. Conclusion

We have shown that the LMCOF delivered a high specific discharge capacity of 253 mAh g^{-1}, a specific energy of 814 Wh kg^{-1}, and a capacity retention of 61.5% after 1000 cycles at 200 mA g^{-1} and 2.0–4.4 V vs Li/Li^+. The trivalent Cr^{3+} in LMCOF, distinct from redox inactive charge compensators in other DRX materials, exhibits high redox activity with good reversibility during cycling. Benefiting from the Mn/Cr dual redox, mitigated oxygen redox, reversible oxygen chemical environment, and stable crystal structure, the LMCOF exhibits good battery performance, especially the cycle life. Our study may represent an important discovery in the DRX family and may shed light on designing dual redox, chemically and structurally stable DRX materials without triggering extensive oxygen redox or release.

Declaration of Competing Interest

The authors declare that they have no known competing financial interests or personal relationships that could have appeared to influence the work reported in this paper.

CRediT authorship contribution statement

Xuerong Zheng: Methodology, Formal analysis, Writing – original draft, Writing – review & editing. **Zhengrui Xu:** Investigation, Methodology. **Shaofeng Li:** Investigation. **Yuxin Zhang:** Investigation. **Jinfeng Zhang:** Methodology. **Chunguang Kuai:** Investigation. **Lei Tao:** Methodology. **Muhammad Mominur Rahman:** Investigation. **Yan Zhang:** Investigation. **Cheng-Jun Sun:** Investigation. **Luxi Li:** Investigation. **Wenbin Hu:** Resources. **Dennis Nordlund:** Investigation. **Jue Liu:** Investigation, Formal analysis. **Yijin Liu:** Investigation. **Feng Lin:** Conceptualization, Formal analysis, Writing – original draft, Writing – review & editing.

Acknowledgements

The work was supported by Virginia Tech Department of Chemistry Startup Funds, the Thomas F. and Kate Miller Jeffress Memorial Trust, Bank of America, Trustee and the Jeffress Trust Awards Program in Interdisciplinary Research, and the National Science Foundation (DMR-2045570). Use of the Stanford Synchrotron Radiation Lightsource, SLAC National Accelerator Laboratory, is supported by the U.S. Department of Energy, Office of Science, Office of Basic Energy Sciences under Contract No. DE-AC02–76SF00515. This research used resources of the Advanced Photon Source, a U.S. Department of Energy (DOE) Office of Science User Facility operated for the DOE Office of Science by Argonne National Laboratory under Contract No. DE-AC02–06CH11357. This research used 28-ID-2 at the National Synchrotron Light Source II, a U.S. Department of Energy (DOE) Office of Science User Facility operated for the DOE Office of Science by Brookhaven National Laboratory under Contract No. DE-SC0012704. Research conducted at Spallation Neutron Source in Oak Ridge National Laboratory was sponsored by the Scientific User Facilities Division, Office of Basic Energy Sciences, U.S. Department of Energy.

Supplementary materials

Supplementary material associated with this article can be found, in the online version, at doi:10.1016/j.actamat.2021.116935.

References

[1] X. Li, Y. Qiao, S. Guo, K. Jiang, M. Ishida, H. Zhou, A new type of Li-rich rock-salt oxide Li2Ni1/3Ru2/3O3 with reversible anionic redox chemistry, Adv. Mater. 31 (11) (2019) 1807825.
[2] R.J. Clément, D. Kitchaev, J. Lee, Gerbrand Ceder, Short-range order and unusual modes of nickel redox in a fluorine-substituted disordered rocksalt oxide lithium-ion cathode, Chem. Mater. 30 (19) (2018) 6945–6956.
[3] S. Hoshino, A.M. Glushenkov, S. Ichikawa, T. Ozaki, T. Inamasu, N. Yabuuchi, Reversible three-electron redox reaction of Mo3+/Mo6+ for rechargeable lithium batteries, ACS Energy Lett 2 (4) (2017) 733–738.
[4] R. Wang, X. Li, L. Liu, J. Lee, D.H. Seo, S.H. Bo, A. Urban, G. Ceder, A disordered rock-salt Li-excess cathode material with high capacity and substantial oxygen redox activity: li1.25Nb0.25Mn0.5O2, Electrochem. Commun. 60 (2015) 70–73.
[5] N. Yabuuchi, M. Takeuchi, S. Komaba, S. Ichikawa, T. Ozaki, T. Inamasu, Synthesis and electrochemical properties of Li1.3Nb0.3V0.4O2 as a positive electrode material for rechargeable lithium batteries, Chem. Commun. 52 (10) (2016) 2051–2054.
[6] D.A. Kitchaev, Z. Lun, W.D. Richards, H. Ji, R.J. Clément, M. Balasubramanian, D.H. Kwon, K. Dai, J.K. Papp, T. Lei, B.D. McCloskey, W. Yang, J. Lee, G. Ceder, Design principles for high transition metal capacity in disordered rocksalt Li-ion cathodes, Energy Environ. Sci. 11 (8) (2018) 2159–2171.
[7] N. Pereira, F. Badway, M. Wartelsky, S. Gunn, G.G. Amatucci, Iron oxyfluorides as high capacity cathode materials for lithium batteries, J. Electrochem. Soc. 156 (6) (2009) A407–A416.
[8] N. Takeda, S. Hoshino, L. Xie, S. Chen, I. Ikeuchi, R. Natsui, K. Nakura, N. Yabuuchi, Reversible Li storage for nanosize cation/anion-disordered rocksalt-type oxyfluorides: liMoO2-xLiF (0 ≤x ≤ 2) binary system, J. Power Sources 367 (2017) 122–129.
[9] L. Zhang, D. Dambournet, A. Iadecola, D. Batuk, O.J. Borkiewicz, K.M. Wiaderek, E. Salager, M. Shao, G. Chen, J.M. Tarascon, Origin of the high capacity manganese-based oxyfluoride electrodes for rechargeable batteries, Chem. Mater. 30 (15) (2018) 5362–5372.
[10] R.A. House, L. Jin, U. Maitra, K. Tsuruta, J.W. Somerville, D.P. Förstermann, F. Massel, L. Duda, M.R. Roberts, P.G. Bruce, Lithium manganese oxyfluoride as a new cathode material exhibiting oxygen redox, Energy Environ. Sci. 11 (4) (2018) 926–932.
[11] S.W. Kim, N. Pereira, N.A. Chernova, F. Omenya, P. Gao, M.S. Whittingham, G.G. Amatucci, D. Su, F. Wang, Structure stabilization by mixed anions in oxyfluoride cathodes for high-energy lithium batteries, ACS Nano 9 (10) (2015) 10076–10084.
[12] J. Lee, A. Urban, X. Li, D. Su, G. Hautier, G. Ceder, Unlocking the potential of cation-disordered oxides for rechargeable lithium batteries, Science 343 (6170) (2014) 519–522.
[13] J. Lee, D.A. Kitchaev, D.H. Kwon, C.W. Lee, J.K. Papp, Y.S. Liu, Z. Lun, R.J. Clément, T. Shi, B.D. McCloskey, J. Guo, M. Balasubramanian, G. Ceder, Reversible Mn2+/Mn4+ double redox in lithium-excess cathode materials, Nature 556 (7700) (2018) 185–190.
[14] H. Ji, A. Urban, D.A. Kitchaev, D.H. Kwon, N. Artrith, C. Ophus, W. Huang, Z. Cai, T. Shi, J.C. Kim, H. Kim, G. Ceder, Hidden structural and chemical order controls lithium transport in cation-disordered oxides for rechargeable batteries, Nat. Commun. 10 (1) (2019) 592.
[15] C.S. Johnson, J.S. Kim, C. Lefief, N. Li, J.T. Vaughey, M.M. Thackeray, The significance of the Li2MnO3 component in "composite" xLi2MnO3 (1-x)LiMn0.5Ni0.5O2 electrodes, Electrochem. Commun. 6 (10) (2004) 1085–1091.
[16] R. Chen, R. Witte, R. Heinzmann, S. Ren, S. Mangold, H. Hahn, R. Hempelmann, H. Ehrenberg, S. Indris, Identifying the redox activity of cation-disordered Li-Fe-V-Ti oxide cathodes for Li-ion batteries, Phys. Chem. Chem. Phys. 18 (11) (2016) 7695–7701.
[17] W.H. Kan, D. Chen, J.K. Papp, A.K. Shukla, A. Huq, C.M. Brown, B.D. McCloskey, G. Chen, Unravelling solid-state redox chemistry in Li1.3Nb0.3Mn0.4O2 single-crystal cathode material, Chem. Mater. 30 (5) (2018) 1655–1666.

[18] H. Ji, D.A. Kitchaev, Z. Lun, H. Kim, E. Foley, D.H. Kwon, Y. Tian, M. Balasubramanian, M. Bianchini, Z. Cai, R.J. Clément, J.C. Kim, G. Ceder, Computational investigation and experimental realization of disordered high-capacity Li-ion cathodes based on Ni redox, Chem. Mater. 31 (7) (2019) 2431–2442.
[19] W.D. Richards, S.T. Dacek, D.A. Kitchaev, G. Ceder, Fluorination of lithium-excess transition metal oxide cathode materials, Adv. Energy Mater. 8 (5) (2018) 1701533.
[20] A. Sakuda, T. Takeuchi, K. Okamura, H. Kobayashi, H. Sakaebe, K. Tatsumi, Z. Ogumi, Rock-salt-type lithium metal sulphides as novel positive-electrode materials, Sci. Rep. 4 (2014) 4883.
[21] N. Yabuuchi, M. Takeuchi, M. Nakayama, H. Shiiba, M. Ogawa, K. Nakayama, T. Ohta, D. Endo, T. Ozaki, T. Inamasu, K. Sato, S. Komaba, High-capacity electrode materials for rechargeable lithium batteries: li3NbO4-based system with cation-disordered rocksalt structure, Proc. Natl. Acad. Sci. U. S. A. 112 (25) (2015) 7650–7655.
[22] S. Ren, R. Chen, E. Maawad, O. Dolotko, A.A. Guda, V. Shapovalov, D. Wang, H. Hahn, M. Fichtner, Improved voltage and cycling for Li+ intercalation in high-capacity disordered oxyfluoride cathodes, Adv. Sci. 2 (10) (2015) 1500128.
[23] A. Urban, A. Abdellahi, S. Dacek, N. Artrith, G. Ceder, Electronic-structure origin of cation disorder in transition-metal oxides, Phys. Rev. Lett. 119 (17) (2017) 176402.
[24] Z. Lun, B. Ouyang, D.A. Kitchaev, R.J. Clément, J.K. Papp, M. Balasubramanian, Y. Tian, T. Lei, T. Shi, B.D. McCloskey, J. Lee, G. Ceder, Improved cycling performance of Li-excess cation-disordered cathode materials upon fluorine substitution, Adv. Energy Mater. 9 (2) (2019) 1802959.
[25] E. Zhao, L. He, B. Wang, X. Li, J. Zhang, Y. Wu, J. Chen, S. Zhang, T. Liang, Y. Chen, X. Yu, H. Li, L. Chen, X. Huang, H. Chen, F. Wang, Structural and mechanistic revelations on high capacity cation-disordered Li-rich oxides for rechargeable Li-ion batteries, Energy Storage Mater 16 (2019) 354–363.
[26] R. Chen, S. Ren, M. Knapp, D. Wang, R. Witter, M. Fichtner, H. Hahn, Disordered lithium-rich oxyfluoride as a stable host for enhanced Li+ intercalation storage, Adv. Energy Mater. 5 (9) (2015) 1401814.
[27] M. Freire, N.V. Kosova, C. Jordy, D. Chateigner, O.I. Lebedev, A. Maignan, V. Pralong, A new active Li-Mn-O compound for high energy density Li-ion batteries, Nat. Mater. 15 (2) (2016) 173–177.
[28] D. Chen, W.H. Kan, G. Chen, Understanding performance degradation in cation-disordered rock-salt oxide cathodes, Adv. Energy Mater. 9 (2019) 1901255.
[29] K. Luo, M.R. Roberts, R. Hao, N. Guerrini, D.M. Pickup, Y.S. Liu, K. Edström, J. Guo, A.V. Chadwick, L.C. Duda, P.G. Bruce, Charge-compensation in 3d-transition-metal-oxide intercalation cathodes through the generation of localized electron holes on oxygen, Nat. Chem. 8 (7) (2016) 684–691.
[30] N. Yabuuchi, M. Nakayama, M. Takeuchi, S. Komaba, Y. Hashimoto, T. Mukai, H. Shiiba, K. Sato, Y. Kobayashi, A. Nakao, M. Yonemura, K. Yamanaka, K. Mitsuhara, T. Ohta, Origin of stabilization and destabilization in solid-state redox reaction of oxide ions for lithium-ion batteries, Nat. Commun. 7 (2016) 13814.
[31] D.H. Seo, J. Lee, A. Urban, R. Malik, S. Kang, G. Ceder, The structural and chemical origin of the oxygen redox activity in layered and cation-disordered Li-excess cathode materials, Nat. Chem. 8 (7) (2016) 692–697.
[32] J. Lee, J.K. Papp, R.J. Clément, S. Sallis, D.H. Kwon, T. Shi, W. Yang, B.D. McCloskey, G. Ceder, Mitigating oxygen loss to improve the cycling performance of high capacity cation-disordered cathode materials, Nat. Commun. 8 (1) (2017) 981.
[33] J. Lee, D.H. Seo, M. Balasubramanian, N. Twu, X. Li, G. Ceder, A new class of high capacity cation-disordered oxides for rechargeable lithium batteries: li-Ni-Ti-Mo oxides, Energy Environ. Sci. 8 (11) (2015) 3255–3265.
[34] H. Koga, L. Croguennec, M. Menetrier, K. Douhil, S. Belin, L. Bourgeois, E. Suard, F. Weill, C. Delmas, Reversible oxygen participation to the redox processes revealed for Li1.20Mn0.54Co0.13Ni0.13O2, J. Electrochem. Soc. 160 (6) (2013) A786–A792.
[35] J. Neuefeind, M. Feygenson, J. Carruth, R. Hoffmann, K.K. Chipley, The nanoscale ordered materials diffractometer NOMAD at the spallation neutron source SNS, Nucl. Instrum. Methods Phys. Res. Sect. B Beam Interact. Mater. Atoms 287 (2012) 68–75.
[36] F. Farges, G.E. Brown, Ti-edge XANES studies of Ti coordination and disorder in oxide compounds: comparison between theory and experiment, Phys. Rev. B Condens. Matter Mater. Phys. 56 (4) (1997) 1809–1819.
[37] H. Modrow, S. Bucher, J.J. Rehr, A.L. Ankudinov, Calculation and interpretation of K-shell *X-ray* absorption near-edge structure of transition metal oxides, Phys. Rev. B Condens. Matter Mater. Phys. 67 (3) (2003) 035123.
[38] M.R. Li, Z. Deng, S.H. Lapidus, P.W. Stephens, C.U. Segre, M. Croft, R. Paria Sena, J. Hadermann, D. Walker, M. Greenblatt, Ba3(Cr0.97(1)Te0.03(1))2TeO9: in search of Jahn-Teller distorted Cr(II) oxide, Inorg. Chem. 55 (20) (2016) 10135–10142.
[39] Y. Lyu, L. Ben, Y. Sun, D. Tang, K. Xu, L. Gu, R. Xiao, H. Li, L. Chen, X. Huang, Atomic insight into electrochemical inactivity of lithium chromate (LiCrO2): irreversible migration of chromium into lithium layers in surface regions, J. Power Sources 273 (2015) 1218–1225.
[40] J.H. Dai, Q. Zhao, Q. Sun, S. Zhang, X. Wang, X.D. Shen, Z.H. Liu, X. Shen, R.C. Yu, T.S. Chan, L.X. Li, G.H. Zhou, Y.F. Yang, C.Q. Jin, Y.W. Long, Formation of unusual Cr5+ charge state in CaCr0.5Fe0.5O3 perovskite, Chin. Phys. B 27 (3) (2018) 037503.
[41] Z. Xia, H. Zhang, K. Shen, Y. Qu, Z. Jiang, Wavelet analysis of extended *X-ray* absorption fine structure data: theory, application, Phys. B Condens. Matter 542 (2018) 12–19.
[42] C. Mikutta, R. Kretzschmar, Spectroscopic evidence for ternary complex formation between arsenate and ferric iron complexes of humic substances, Environ. Sci. Technol. 45 (22) (2011) 9550–9557.
[43] M.D. De Jonge, S. Vogt, Hard *X-ray* fluorescence tomography-an emerging tool for structural visualization, Curr. Opin. Struct. Biol. 20 (5) (2010) 606–614.
[44] J. Rodríguez-Carvajal, G. Rousse, C. Masquelier, M. Hervieu, Electronic crystallization in a lithium battery material: columnar ordering of electrons and holes in the spinel LiMn2O4, Phys. Rev. Lett. 81 (21) (1998) 4660–4663.
[45] W.S. Yoon, C.P. Grey, M. Balasubramanian, X.Q. Yang, J. McBreen, In situ X-ray absorption spectroscopic study on LiNi0.5Mn0.5O2 cathode material during electrochemical cycling, Chem. Mater. 15 (16) (2003) 3161–3169.
[46] Y. Terada, K. Yasaka, F. Nishikawa, T. Konishi, M. Yoshio, I. Nakai, situ XAFS analysis of Li(Mn, M)2O4 (M=Cr, Co, Ni) 5V cathode materials for lithium-ion secondary batteries, J. Solid State Chem 156 (2) (2001) 286–291.
[47] Z. Li, F. Du, X. Bie, D. Zhang, Y. Cai, X. Cui, C. Wang, G. Chen, Y. Wei, Electrochemical kinetics of the Li[Li0.23Co0.3Mn0.47] O2 cathode material studied by GITT and EIS, J. Phys. Chem. C. 114 (51) (2010) 22751–22757.
[48] S. Li, S.J. Lee, X. Wang, W. Yang, H. Huang, D.S. Swetz, W.B. Doriese, G.C. OO'Neil, J.N. Ullom, C.J. Titus, K.D. Irwin, H.K. Lee, D. Nordlund, P. Pianetta, C. Yu, J. Qiu, X. Yu, X.Q. Yang, E. Hu, J.S. Lee, Y. Liu, Surface–to-bulk redox coupling through thermally driven Li redistribution in Li- and Mn-rich layered cathode materials, J. Am. Chem. Soc. 141 (30) (2019) 12079–12086.
[49] L. Tao, Z. Xu, C. Kuai, X. Zheng, C.E. Wall, C. Jiang, A.R. Esker, Z. Zheng, F. Lin, Flexible lignin carbon membranes with surface ozonolysis to host lean lithium metal anodes for nickel-rich layered oxide batteries, Energy Storage Mater 24 (2019) 129–137.
[50] G. Assat, D. Foix, C. Delacourt, A. Iadecola, R. Dedryvère, J.M. Tarascon, Fundamental interplay between anionic/cationic redox governing the kinetics and thermodynamics of lithium-rich cathodes, Nat. Commun. 8 (1) (2017) 2219.
[51] M. Munoz, P. Argoul, F. Farges, Continuous cauchy wavelet transform analyses of EXAFS spectra: a qualitative approach, Am. Mineral. 88 (4) (2003) 694–700.
[52] J. Timoshenko, A. Kuzmin, Wavelet data analysis of EXAFS spectra, Comput. Phys. Commun. 180 (6) (2009) 920–925.
[53] J.N. Zhang, Q. Li, C. Ouyang, X. Yu, M. Ge, X. Huang, E. Hu, C. Ma, S. Li, R. Xiao, W. Yang, Y. Chu, Y. Liu, H. Yu, X.Q. Yang, X. Huang, L. Chen, H. Li, Trace doping of multiple elements enables stable battery cycling of LiCoO2 at 4.6V, Nat. Energy 4 (7) (2019) 594–603.
[54] J. Xu, M. Sun, R. Qiao, S.E. Renfrew, L. Ma, T. Wu, S. Hwang, D. Nordlund, D. Su, K. Amine, J. Lu, B.D. McCloskey, W. Yang, W. Tong, Elucidating anionic oxygen activity in lithium-rich layered oxides, Nat. Commun. 9 (1) (2018) 947.
[55] Z.W. Lebens-Higgins, N.V. Faenza, M.D. Radin, H. Liu, S. Sallis, J. Rana, J. Vinckeviciute, P.J. Reeves, M.J. Zuba, F. Badway, N. Pereira, K.W. Chapman, T.L. Lee, T. Wu, C.P. Grey, B.C. Melot, A. Van Der Ven, G.G. Amatucci, W. Yang, L.F.J. Piper, Revisiting the charge compensation mechanisms in LiNi0.8Co0.2yAlyO2 systems, Mater. Horiz. 6 (2019) 2112–2123.
[56] D. Liu, Z. Shadike, R. Lin, K. Qian, H. Li, K. Li, S. Wang, Q. Yu, M. Liu, S. Ganapathy, X. Qin, Q.H. Yang, M. Wagemaker, F. Kang, X.Q. Yang, B. Li, Review of recent development of in situ/operando characterization techniques for lithium battery research, Adv. Mater. 31 (2019) 1806620.
[57] L. Mu, R. Lin, R. Xu, L. Han, S. Xia, D. Sokaras, J.D. Steiner, T.C. Weng, D. Nordlund, M.M. Doeff, Y. Liu, K. Zhao, H.L. Xin, F. Lin, Oxygen release induced chemomechanical breakdown of layered cathode materials, Nano Lett 18 (5) (2018) 3241–3249.
[58] F. Lin, I.M. Markus, D. Nordlund, T.C. Weng, M.D. Asta, H.L. Xin, M.M. Doeff, Surface reconstruction and chemical evolution of stoichiometric layered cathode materials for lithium-ion batteries, Nat. Commun. 5 (2014) 3529.
[59] J. Hong, H.D. Lim, M. Lee, S.W. Kim, H. Kim, S.T. Oh, G.C. Chung, K. Kang, Critical role of oxygen evolved from layered Li-Excess metal oxides in lithium rechargeable batteries, Chem. Mater. 24 (14) (2012) 2692–2697.
[60] L. Mu, X. Feng, R. Kou, Y. Zhang, H. Guo, C. Tian, C.J. Sun, X.W. Du, D. Nordlund, H.L. Xin, F. Lin, Deciphering the cathode-electrolyte interfacial chemistry in sodium layered cathode materials, Adv. Energy Mater. 8 (34) (2018) 1801975.
[61] N. Takeda, I. Ikeuchi, R. Natsui, K. Nakura, N. Yabuuchi, Improved electrode performance of lithium-excess molybdenum oxyfluoride: titanium substitution with concentrated electrolyte, ACS Appl. Energy Mater. 2 (2019) 1629–1633.
[62] B. Huang, R. Wang, Y. Gong, B. He, H. Wang, Enhanced cycling stability of cation disordered rock-salt Li1.2Ti0.4Mn0.4O2 material by surface modification with Al2O3, Front. Chem. 7 (2019) 107.
[63] M. Murase, J.F. Watts, XPS study of coating delamination from non-rinse chromate treated steel, J. Mater. Chem. 8 (4) (1998) 1007–1018.
[64] J.P. Lafleur, E.D. Salin, Speciation of chromium by high-performance thin-layer chromatography with direct determination by laser ablation inductively coupled plasma mass spectrometry, Anal. Chem. 80 (17) (2008) 6821–6823.
[65] F. Zhou, M. Cococcioni, C.A. Marianetti, D. Morgan, G. Ceder, First-principles prediction of redox potentials in transition-metal compounds with LDA+U, Phys. Rev. B Condens Matter Mater. Phys. 70 (23) (2004) 235121.
[66] C. Liu, Z.G. Neale, G. Cao, Understanding electrochemical potentials of cathode materials in rechargeable batteries, Mater. Today 19 (2) (2016) 109–123.
[67] D.A. Kuznetsov, B. Han, Y. Yu, R.R. Rao, J. Hwang, Y. Román-Leshkov, Y. Shao-Horn, Tuning redox transitions via inductive effect in metal oxides and complexes, and implications in oxygen electrocatalysis, Joule 2 (2) (2018) 225–244.